Journal of The Electrochemical Society

OPEN ACCESS

Understanding the Electrooxidation of Dimethyl Ether on $Pt_3Pd_3Sn_2$ Supported on a Mixture of Carbon Materials

To cite this article: Medhanie Gebremedhin *et al* 2023 *J. Electrochem. Soc.* **170** 114509

Journal of The Electrochemical Society, 2023 **170** 114509

Understanding the Electrooxidation of Dimethyl Ether on $Pt_3Pd_3Sn_2$ Supported on a Mixture of Carbon Materials

Medhanie Gebremedhin,[1] Hannan Teller,[1,*] and Alex Schechter[1,2,z,*]

[1]*Department of Chemical Sciences, Ariel University, Ariel, 40700, Israel*
[2]*Research and Development Centre for Renewable Energy, New Technology Centre, West Bohemia University, West Bohemia in Pilsen, Czech Republic*

Recently, we reported a rigorous study on the effect of carbon supports and their cold plasma treatment on a state-of-the-art catalyst, $Pt_3Pd_3Sn_2$, for dimethyl ether (DME) electrooxidation. The catalyst supported on a mixture of 75% activated multi-walled carbon nanotube (MWCNT) (75 M) and 25% pristine black pearl 2000 (BP2000) (25B) ($Pt_3Pd_3Sn_2$/75M25B) offered improved DME kinetics with respect to the single or other combinations of the same supports. In this work, the results of the electrochemical impedance spectroscopy (EIS) were coupled with physicochemical characterizations (X-ray Diffraction (XRD), Small Angle X-ray Scattering (SAXS), and Scanning Tunneling Electron Microscopy (STEM)) for a detailed understanding of the origins of the improved kinetics. With an appropriate composition of the two supports in the mixture (75M25B), a catalyst with optimized particle size, dispersion, and conductivity was obtained. A $Pt_3Pd_3Sn_2$/75M25B-coated electrode exhibited a reduced charge transfer resistance of 0.63 ohms at the catalyst layer compared to BP2000 and MWCNT, which showed 1.53 and 1.31 ohms, respectively. These results provide vital insights into catalyst support design considering the use of support mixtures of optimized conductivity and surface area for enhanced power output.
 [DOI: 10.1149/1945-7111/ad07fe]

Manuscript submitted March 6, 2023; revised manuscript received June 13, 2023. Published November 8, 2023.

The various advantages that dimethyl ether (DME) offers over other small organic molecules recently led to extensive research on direct DME fuel cells (DDMEFCs). DME is easy to store and transport in a liquid form at low pressure (5 atm). It also provides a high energy density of 8.1 kW kg^{-1} and has reduced Nafion membrane crossover, thereby minimizing the cathode mixed potential.[1–3] However, the need for high loading of precious metals has been one of the challenging issues that prohibited the DDMEFCs application. Alloying the noble metals with other relatively low-cost metals, choosing the best catalyst support, and improving the catalyst's utilization have been adopted by many studies to improve the power output of these cells while reducing the content of the noble metal.[3–8] Carbons are the leading supporting materials for fuel cell catalysts, owing to their chemical stability, electronic conductivity, and improved particle dispersion, thus lowering the catalyst loading while maintaining high power density.

The commonly used carbon supports include Vulcan XC72,[9] carbon cryogel,[10] carbon aerogel,[11] single and multi-walled carbon nanotubes (SWCNT and MWCNT),[12] and black pearl 2000 (BP2000).[13] Among the selected supporting materials, BP2000 and CNTs have gained substantial attention due to their high surface area, conductivity, and chemical stability.[14,15]

In a fuel cell, fast charge transfer kinetics is essential to sustain high power output that depends on the type of platinum-based catalysts as well as on the dispersion of the catalyst particles on the support, its porous structure, and the thickness of the catalyst layer coated on the electrode.[16–18] Facil charge transfer kinetics also depend upon the surface adsorbed oxidation intermediates,[19] fuel concentration,[20] and the working electrode applied potential.[20] Electrochemical impedance spectroscopy (EIS) is an excellent tool to determine the various charge and mass transfer-related impedances that hinder the flow of electrons and ions and to analyze the reaction kinetics at the electrode and electrode-electrolyte interface.[21]

In our previous study,[22] we have shown a highest reported performance of a ternary metal catalyst ($Pt_3Pd_3Sn_2$) supported on a mixture of 75% multi-walled carbon nanotube (75 M) and 25% black pearl 2000 (25B) towards DME oxidation. The primary objective of this work is, therefore, to further understand the influence of the combined properties of the carbon mixture on the impedances and capacitances present at the catalyst layer and electrode-electrolyte interface during dimethyl ether (DME) electrooxidation. The electrode used was a Toray paper coated with $Pt_3Pd_3Sn_2$ supported on pure and mixtures of plasma-treated MWCT and pristine BP2000 ($Pt_3Pd_3Sn_2$/xM(100-x)B (x = 25–-100)). In addition, X-ray diffraction (XRD), small-angle X-ray scattering (SAXS), and scanning tunneling electron microscopy (STEM) measurements were performed to assess the effect of particle size, structure, and morphology of the catalyst particles due to varying the composition of the binary carbon supports.

Materials and Methodology

Catalysts synthesis.—The $Pt_3Pd_3Sn_2$/xM(100-x)B (x = 25–100, M = MWCNT, and B = BP2000) catalysts were synthesized following the procedure elucidated in the literature by Kashyap et al.[21] In short, the metal precursors, K_2PtCl_4, $PdCl_2$, and $SnCl_2$, were dissolved separately in ethylene glycol. The solution was mixed with either ethylene glycol-dispersed pure or a mixture of MWCNT and BP2000 supports and stirred overnight. The mixture was refluxed at 180 °C–200 °C for two hours after adjusting its pH to 12 with the addition of NaOH. After cooling the solution to room temperature, the catalyst was washed several times with a mixture of acetone and distilled water collected by centrifugation and dried.

Physical characterizations.—X-ray diffraction (XRD) measurements were done using a Rigaku SmartLab diffractometer equipped with a DteX250(H) detector and a CuKα rotating anode X-ray generator. Conditions used were a wavelength, λ, of 1.54 Å and a 3 kW max. load operating at 40 kV and 45 mA. The XRD pattern was recorded between 2θ = 10° and 100° at a scan speed of 0.1 degrees/min. Transmission small-angle X-ray scattering (SAXS) (SmartLab, Rigaku) analysis of the catalysts was conducted to determine the effect of the supports on the size and distribution of the particles. The sample was scanned in the range between 0.6° – 2° at an interval of 0.05°. The X-ray source and detector used for the SAXS and XRD were the same. An image of the catalysts was taken using a scanning tunneling electron microscope (STEM) (Tescan MAIA3 Triglav™, Brno-Kohoutovice) to visualize the surface morphology and particle dispersion.

*Electrochemical Society Member.
[z]E-mail: salex@ariel.ac.il

Electrochemical impedance spectroscopy.—Impedance spectra were measured in a conventional three-electrode cell using a graphite rod, Ag/AgCl electrodes, and catalyst-coated non-teflonized carbon paper as a counter, reference, and working electrodes, respectively. To prepare the ink, 4 mg of the catalyst mixed with 20 μl of aqueous Nafion solution (5% in aliphatic alcohol) (20% of the catalyst powder) was dispersed in a 1 ml mixture of isopropyl alcohol and distilled water (1:1, V/V). A 25 μl aliquot of this suspension was coated on a 1 cm^2 electrode making the loading 100 ug cm^{-2}, also verified by the dry weight change. All the potentials are expressed versus a normal hydrogen electrode (NHE) reference electrode. The potential of the Ag/AgCl (4 M KCl), used when performing the electrochemical measurements, was first compared with the normal hydrogen electrode and was nearly 0.214 mV higher. Hence, this offset potential was subtracted from the measured potentials using Ag/AgCl reference electrode to convert it to NHE using Eq. 1. The Nyquist plot was recorded from 200 kHz to 10 m Hz with 6 frequencies per decade and 10 mV amplitude using an electrochemical workstation (BioLogic VSP) at selected bias potentials.

$$E(NHE) = E(Ag/AgCl) - 0.214\ V \quad [1]$$

Fitting the EIS data with a selected equivalent electric circuit (EEC) model was performed by the Zfit function from the EC-lab software (version 11.33), as shown in Fig. 1. For a better fitting, a high iteration number (>20000) was used. The iterative method chosen to minimize the fitting criteria, X^2/|Z|, was a randomized + simplex method.[23] The randomization tool helps to select a suitable set of initial values that are very close to the real values that would yield the lowest possible X^2/|Z|.

The total impedance, Z, of the equivalent circuit shown in Fig. 1 which is used to fit the EIS data discussed in the later sections, is given by Eq. 2

$$Z = R_s + \frac{R_f}{R_f Q_f (j\omega)^{a_1} + 1} + \frac{R_{ct}}{R_{ct} Q_{dl} (j\omega)^{a_2} + 1} + \sigma\omega^{-1/2}(1 - j) \quad [2]$$

Where R_s is the solution resistances, $R_f \| Q_f$ (R_f and Q_f connected in parallel) is the combination of the resistance and capacitance at the catalyst film layer, and $R_{ct} \| Q_{dl}$ is the charge transfer resistance and double-layer capacitance at the electrode surface/electrolyte interface. A detailed physical description of these circuit elements is provided in the subsequent sections. a_1 and a_2 are exponents for Q_f and Q_{dl} to account for the roughness of the electrode surface. ω is the frequency and σ is the Warburg impedance coefficient which can be calculated using Eq. 3.

$$\sigma = \frac{RT}{\sqrt{2}n^2F^2}\left[\frac{1}{C_{ox}D_{ox}^{1/2}} - \frac{1}{C_{red}D_{red}^{1/2}}\right] \quad [3]$$

Where *R, T, n, and F* are the ideal gas constant, absolute temperature, the number of electrons transferred, and Faraday's constant, respectively. *C* and *D* are the concentration and diffusion coefficient, respectively, of the oxidation and reduction species.

Equation 2 could be resolved into the real and imaginary impedance components (Z_{re} and Z_{im}, respectively) as shown in Eqs. 4 and 5

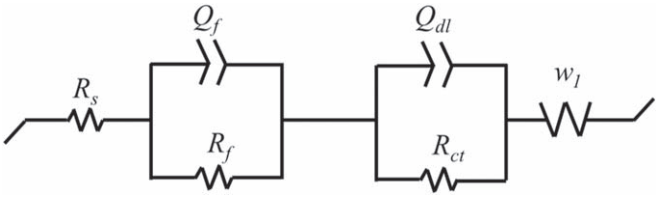

Figure 1. Equivalent circuit of the Nyquist plot for the catalysts.

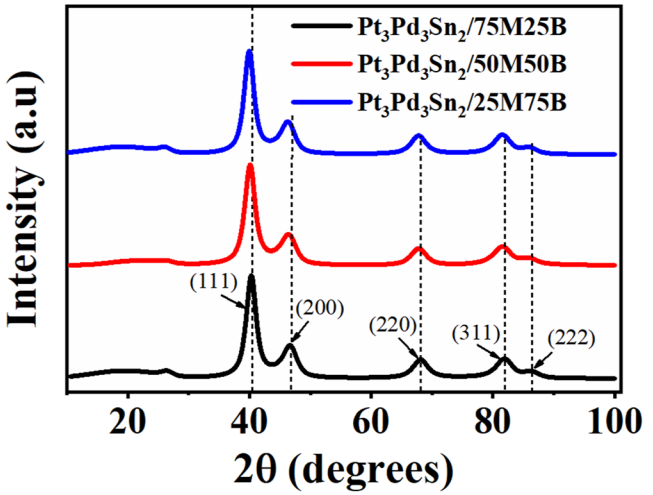

Figure 2. (a) X-ray diffraction patterns of the $Pt_3Pd_3Sn_2$ catalyst supported on the mixture of BP2000 and MWCNT carbon supports.

$$Z_{re} = R_s + \frac{R_f\left(1 + R_f Q_f \omega^{a_1} \cos\frac{a_1\pi}{2}\right)}{1 + (R_f Q_f \omega^{a_1})^2 + 2R_f Q_f \omega^{a_1} \cos\frac{a_1\pi}{2}} + \frac{R_{ct}\left(1 + R_{ct} Q_{dl} \omega^{a_2} \cos\frac{a_2\pi}{2}\right)}{1 + (R_{ct} Q_{dl} \omega^{a_2})^2 + 2R_{ct} Q_{dl} \omega^{a_2} \cos\frac{a_2\pi}{2}} + \sigma\omega^{-1/2} \quad [4]$$

$$Z_{im} = -\frac{R_f\left(1 + R_f Q_f \omega^{a_1} \sin\frac{a_1\pi}{2}\right)}{1 + (R_f Q_f \omega^{a_1})^2 + 2R_f Q_f \omega^{a_1} \cos\frac{a_1\pi}{2}} - \frac{R_{ct}\left(1 + R_{ct} Q_{dl} \omega^{a_2} \sin\frac{a_2\pi}{2}\right)}{1 + (R_{ct} Q_{dl} \omega^{a_2})^2 + 2R_{ct} Q_{dl} \omega^{a_2} \cos\frac{a_2\pi}{2}} + j\sigma\omega^{-1/2} \quad [5]$$

Results and Discussion

Physicochemical characterizations.— *X-ray diffraction.*— Shown in Fig. 2 are the X-ray diffraction patterns of the $Pt_3Pd_3Sn_2$ catalyst supported on the carbon support mixture. These peaks were matched well with the Atokite phase (PDF 1522890), which has the chemical formula of $(PtPd)_{1.5}Sn$. The XRD peaks for this phase appear at 2θ of 39.03°, 45.38°, 66.13°, 79.54°, and 83.85°. The main characteristic peaks of the catalyst at these angles correspond to the Miller Index of (111), (200), (220), (311), and (222). The catalysts have a face-centered cubic (FCC) crystal structure with a space group of Pm-3m. Relative to this phase, the peaks for the catalysts showed a 1 – 1.5° shift towards higher

angles. The positive shift in 2θ was ascribed to the decrease in the size of the unit cell according to Brags law.[24]

In our previous study, the XRD pattern for the catalyst supported on pure MWCNT and BP2000 was reported.[22] $Pt_3Pd_3Sn_2$/BP2000 had an average crystallite size of 3.67 nm, smaller than that of $Pt_3Pd_3Sn_2$/MWNCT (5.70 nm) due to the growth of the nanoparticles in the confined small pores of the BP2000. This was evidenced by the pore size analysis using N_2 adsorption in our previous study. Unlike MWCNT, which showed no change in the N_2-gas uptake following the incorporation of the particles, BP2000 showed a significant decrease. In this case, the strong metal-support interaction pulls the metal layers toward the interface and decreases the crystallite size. The high surface area of BP2000, which enabled it to have better contact with the particles and the insertion of some of the metal particles into the pores of this support, strengthens the metal-support interactions.[25] In the mixture of these supports, the X-ray peaks shifted towards lower 2θ as the MWCNT content increased, indicating an increase in the unit cell dimensions. Therefore, MWCNT's role in the support mixture is not in obtaining smaller-sized particles. It was reported that the particle size effect on the oxidation of organic molecules is associated with the difference in the Pt-CO and Pt-OH bond strengths.[26] Small-sized particles have higher oxygen affinity than larger ones hence they contain more Pt-OH species via water activation (session of H-O-H bonds) at lower potential. These -OH species help to oxidize the poisoning CO_{ads}. However, with a further decrease in the particle size below the range of about 4.5 nm, the number of reactive species adsorption sites is limited due to the high surface coverage of the hydroxide as well as other metal oxides.[27] Therefore, for better catalyst performance, optimizing the particle size is highly essential. The highest DME anodic currents were observed with $Pt_3Pd_3Sn_2$/75M25B of an average crystallite size (D) of 4.18 nm, calculated by Scherrer's Eq. 6 from the peak assigned to the 220 planes, as was done for the single supports.

$$D = \frac{k.\lambda}{\beta.\cos\theta} \qquad [6]$$

Where k, λ, β, and θ are the shape factor (0.89), radiation wavelength, full width at half maximum intensity (FWHM) of (220) plane, and Brag's angle, respectively.

Scanning tunneling electron microscope.—Figure 3 shows STEM images of the catalyst supported on pure and a mixture of carbon supports. Even though the dispersion of the particles on BP2000 was not excellent considering its high surface area, it was still better than on MWCNT which showed local particle agglomerations. Agglomeration of nanoparticles on MWCNT is presumably due to the high tendency of the tubes to adhere to each other and agglomerate.[28] When using black carbons, agglomeration happens only where particles are exposed (not embedded in the micropores). It can be observed in Fig. 3 that the composite of these two supports did not improve the dispersion of the metal particles and was exacerbated by an increase in the MWCNT content. The poor dispersion of the catalyst on the MWCNT support resulted in an inhomogeneous surface, evidenced by the value of the capacitance exponents as explained in the EIS section. Therefore, the best performance exhibited with higher MWCNT content in the support mixture (75M25B) is associated with having better exposed metallic active sites, rather than due to improved dispersion of the catalyst on the support.[29]

The particle size for the nanoparticles supported on selected supports was calculated by taking more than 100 randomly picked nanoparticles from the STEM images and a histogram showing the particle size distribution (PSD) is displayed in Figs. 3f–3h. The average particle size calculated from the STEM was correlated with the crystallite size determined by the XRD and didn't show a significant difference. For the $Pt_3Pd_3Sn_2$/75M25B, these values are 4.31 and 4.18 nm, respectively.

Small-angle X-ray scattering (SAXS).—The PSD of the metal particles supported on different carbon supports as measured by SAXS is displayed in Fig. 4. NANO Solver software was utilized to analyze the SAXS experimental PSD data. An apparent difference in particle size is seen, although the overall particle distribution lies in nearly the same range for all the catalysts. The largest average particle size of 15.85 nm and maximum probability of 4.95 nm was obtained for $Pt_3Pd_3Sn_2$/MWCNT. Moreover, the shift of the PSD curve towards higher particle diameter indicated that the particles for the MWCNT-supported catalyst were relatively large compared to the particles on the other supports. Particles formed on the sidewalls surfaces of the MWCNT tubes tend to aggregate into large particles (Fig. 3a). On the other hand, $Pt_3Pd_3Sn_2$/BP2000 showed particles with a smaller average size of 13.2 nm and a maximum probability of 3.87 nm and has a relatively narrower PSD. The trend that the average particle size increases with the increase in the MWCNT content in the support mixture (Fig. 4b) is in line with the one calculated from the XRD with the values showing only minor differences.

The background-corrected transmission SAXS profile for the catalysts is displayed in Fig. 5a. The corresponding fits included in the curves were generated assuming that the particles were spherical, as was indicated by the excellent fitting of the data with the simulated curves. It can be seen that for all the catalysts, the scattering intensity is convex downward, which is typical of a sample with a broad PSD.[30] This was confirmed from the PSD curve for these catalysts in Fig. 4a. Figure 5b shows the SAXS profile of intensity (I) vs scattering vector (q) at the low q region. The value of q was obtained using Eq. 7

$$q = \frac{4\pi \sin\theta}{\lambda} \qquad [7]$$

Over the entire low q region, the I of the catalyst supported on MWCNT was the highest. Wu et al.,[31] reported that an increase in I, especially at a lower q region of the SAXS profile, is an indication of particles with large sizes which verifies the larger size of the MWCNT-supported particles. The nonlinearity of I vs q at low q (Fig. 5b) arises from the interference of radiation scattered by particles that are very close to each other at a distance smaller than their individual particle size.[32] As a result, the increase in the nonlinearity of the I vs q curves with the increase of MWCNT content in the mixture is an additional confirmation of particle agglomeration. Therefore, the better dispersion of the particles exhibited in $Pt_3Pd_3Sn_2$/75M25B than on MWCNT shown in Fig. 3e is due to the contribution of the 25% BP2000 added. The more pronounced oscillation (more scattered wave) at the high q region observed by $Pt_3Pd_3Sn_2$/25M75B indicates its comparatively narrow particle distribution (Fig. 4a). Conversely, the broad distribution of $Pt_3Pd_3Sn_2$/MWCNT particles was noticed from its obtained relatively monotonous curve.

Electrochemical impedance spectroscopy.—Shown in Fig. 6 is the Nyquist plot recorded from 200 kHz to 10 m Hz at 0.8 V (vs NHE) with 6 frequencies per decade and 10 mV amplitude in DME-saturated 0.5 M H_2SO_4 using a $Pt_3Pd_3Sn_2$/75M25B anode catalyst. In the catalyzed electrode, there may exist more interfaces such as Toray paper-catalyst particles, carbon-metal alloy, catalyst particles-Nafion. The catalyst and Nafion solution were mixed by vigorous stirring during the catalyst ink preparation. Hence, the differences in the time charge transfer constants of these interfaces are beyond the detection limit of our measurement. Therefore, we have labeled these interfaces as one term, the catalyst layer. a Voigt-type equivalent circuit having two time constants (τ = RC) (Fig. 1) was selected to fit the spectra and the values of the circuit elements are summarized in Table I. It should be noted that the simulated curves seem to fit well with our experimental data using the proposed equivalent circuit. The statistical relative deviation, $X^2/|Z|$, was very low (see Tables I, III). The Nyquist plot of the

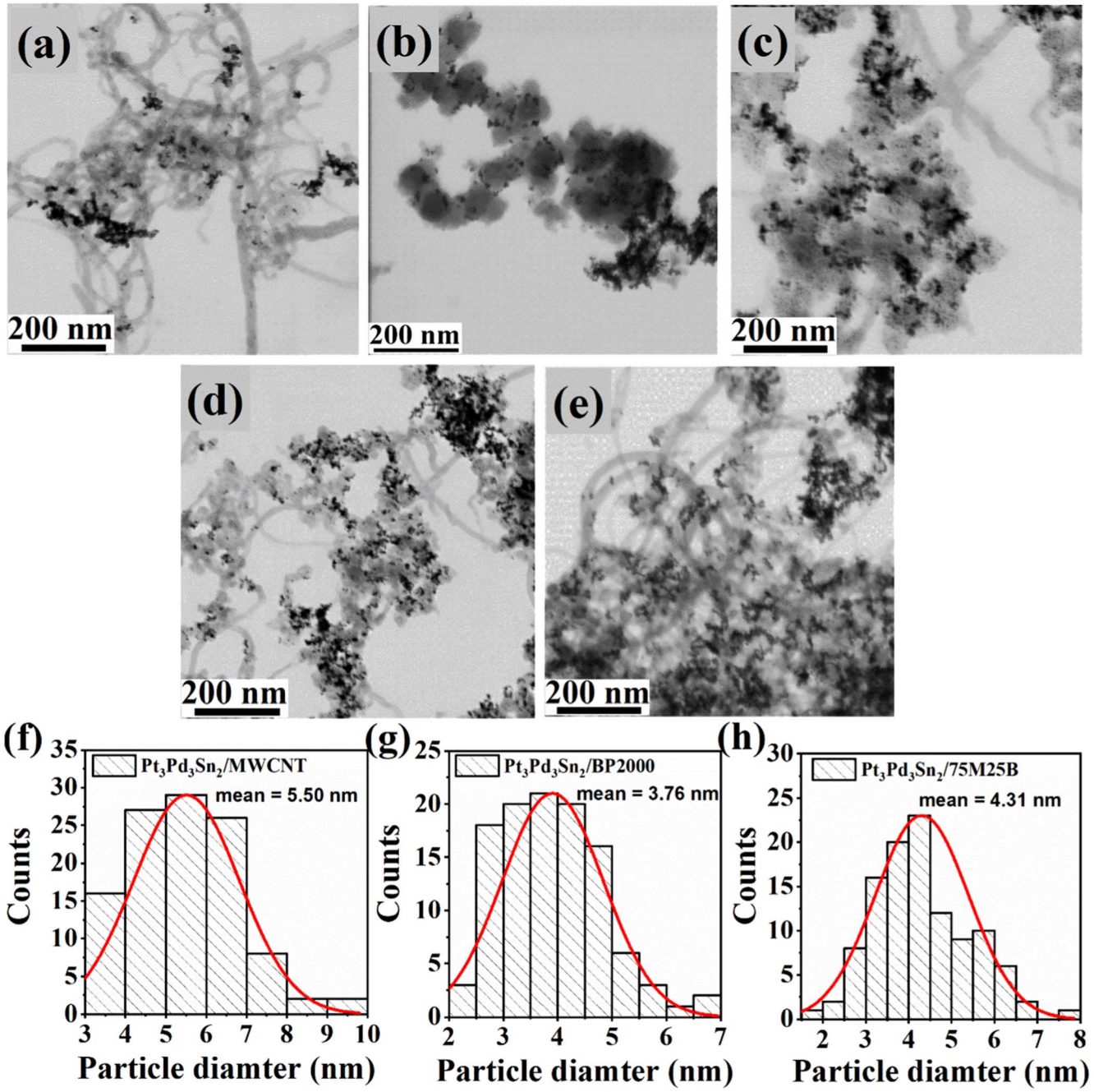

Figure 3. STEM image for (a) $Pt_3Pd_3Sn_2$/MWCNT (b) $Pt_3Pd_3Sn_2$/BP2000 (c) $Pt_3Pd_3Sn_2$/25M75B (d) $Pt_3Pd_3Sn_2$/50M50B and (e) $Pt_3Pd_3Sn_2$/75M25B. (f), (g), and (h) histogram showing PSD of $Pt_3Pd_3Sn_2$ supported on MWCNT, BP2000, and 75M25B, respectively.

catalyst supported on all the carbons consisted of two semicircles; one at high frequency and the other at the high to low-frequency range; and an inclined straight line at a slope of nearly 45°. The intercept of the real part of the impedance at the beginning of the first semicircle (Inset of Fig. 6a) is ohmic resistance corresponding to the electrolyte resistance to the flow of ions (R_s). This parameter value did not show a significant difference among the catalysts.

The first small semicircle, visible by zooming of the high-frequency region, appears at all potentials and is regardless of the presence or absence of DME in the solution, as discussed in the following sections. This suggests that it is not related to the DME oxidation reaction. Moreover, this semicircle is also present in unsupported catalyst and catalyst-free supports-coated electrodes (Fig. 6c; a portion of the Nyquist plot at the high-frequency region is displayed for clarity). This semicircle is related to the resistance due to the H^+ and $SO_4{}^+$ transport limitation through the carbon/Nafion or metal/Nafion film (R_f).[33] It can be seen from Fig. 6c that the diameter of the first semi-circle is lower for metal-free carbon-coated electrodes than for the unsupported catalyst-coated electrode, due to the proton conductivity enhancement by the hydrophilic quinone/hydroquinone redox groups of the carbon material. Generally, relative to the single carbons, a smaller R_f was obtained when a mixture of carbons was used as support. This can be ascribed to the increase in the number of catalyst layer components. The lowest R_f (0.63 Ohm) was found in a mixture of MWCNT and BP2000 carbon supports with a relatively high MWCNT content (75M25B). We ascribed this low resistance to a more uniform and optimal distribution of the pores within the catalyst layer of large irregular MWCNT bundles connected by Van der Walls interactions and

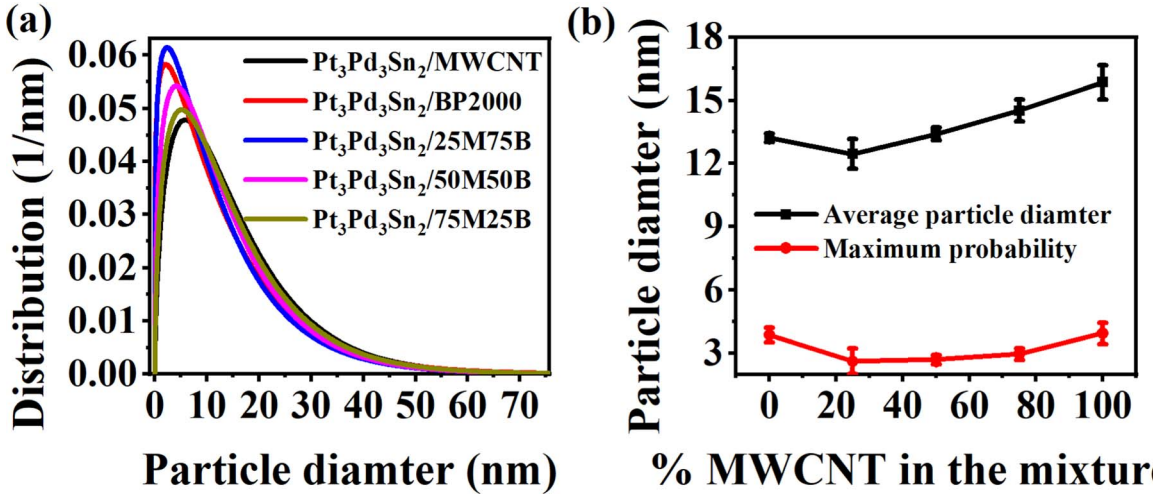

Figure 4. (a) PSD of the catalyst supported on different carbons (b) particle size as a function of MWCNT content in the MWCNT+BP2000 mixture support.

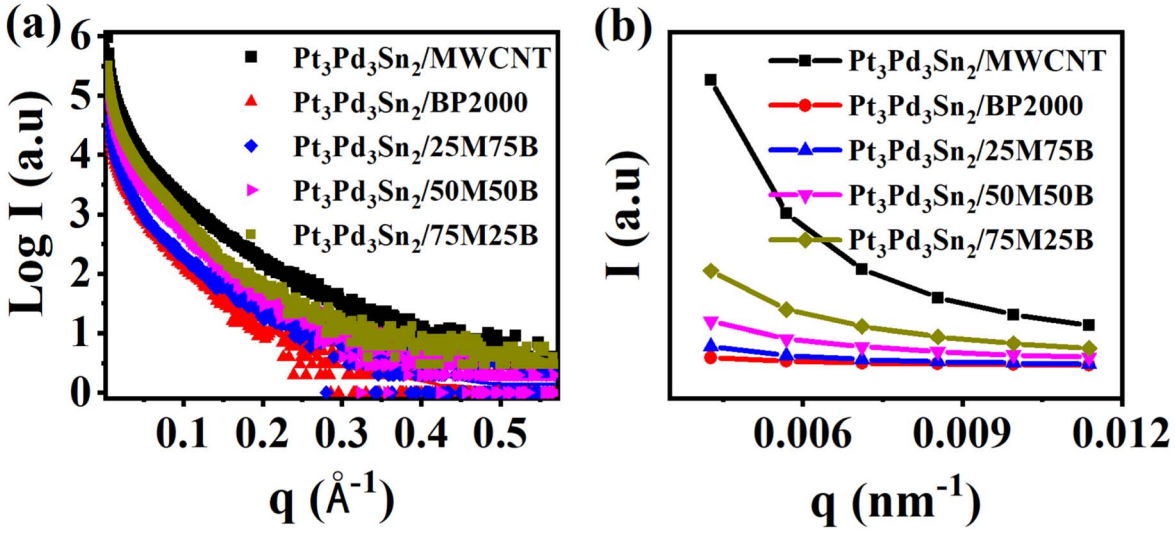

Figure 5. (a) Transmission SAXS profile of the catalyst supported on pure and mixture of carbons. and (b) SAXS profile at the low-q region.

small BP2000 particles acting as spacers, thus providing opening paths for charge transfer between the elongated CNTs and metals.

The second and larger semicircle appeared at the high-to-low frequency range (50 kHz - 100 mHz), only in the presence of DME in the electrolytes, hence representing the charge transfer resistance related to the adsorption of DME oxidation intermediates such as CO_{ads}, CH, OCH_3, and formic acid on the electrode/electrolyte interface (R_{ct}).[34] The R_{ct} was highly affected by the selected carbon support materials. The lowest R_{ct} for $Pt_3Pd_3Sn_2$/75M25B (220 Ohm cm^{-2}) corresponds to faster charge transfer kinetics at the electrode/electrolyte interface associated with fewer DME poisoning oxidation intermediate species at 0.8 V. In our previous study,[22] we observed that relative to the other studied supports, the 75M25B-supported catalyst exhibited the lowest onset potential and highest current density during the stripping of the pre-adsorbed CO monolayer. Therefore, the lowest R_{ct} value of this catalyst shows that the support material played a paramount role in removing the CO_{ads} from $Pt_3Pd_3Sn_2$.

The capacitive impedances at the first and second semicircles are fitted to the equivalent circuit shown in Fig. 1 in terms of constant phase element (CPE) coefficients (Q_f and Q_{dl}, respectively) to account for the inhomogeneity of the porous electrode surface. The porous nature of the catalyst layer film is confirmed by the values of CPE exponents (a_1 and a_2) not being unity. However, the values of a_1 and a_2 being in the range of 0.80–0.98 suggest that the electrode surface heterogeneity was minimal.[35] Comparatively, the a_1 and a_2 values for $Pt_3Pd_3Sn_2$/BP2000 were the largest which indicates that the surface was relatively smooth. Capacitive impedances attributed to the dielectric property of the surface-immobilized film (Q_{dl})[36] show the highest (2.83×10^{-2} F) value for 75M25B supports, in agreement with the highest DME oxidation charge (2015.3 ± 107.7 mC) obtained with the catalyst supported on this support mixture.[22] The Nyquist plot also shows an inclined straight line with a slope of nearly 45° at the low-frequency region of 100 to 10 m Hz which is typical in the EIS of a porous film. This line is the Warburg impedance (W_1) assigned to the mass-transfer resistance of the surface-active species. W_1 is almost equal for all the catalysts. The slight variation in W_1 values could be ascribed to lateral diffusion of DME or oxidation intermediate on $Pt_3Pd_3Sn_2$ confined in the small pores of BP2000.

The phase angle and impedance module are shown in Fig. 6b. Phase angle plot can be a reference to clarity and support the semicircles of a Nyquist plot. The two peaks of the phase angle that are shown at the high and low-frequency regions (30 kHz and 3 Hz, respectively) correspond to the two semi-circles shown in the Nyquist plot (Fig. 6a). The maximum phase angle appearing at the middle-lower frequency region increases and shifts towards a lower frequency values with an increase in the MWCNT content in the

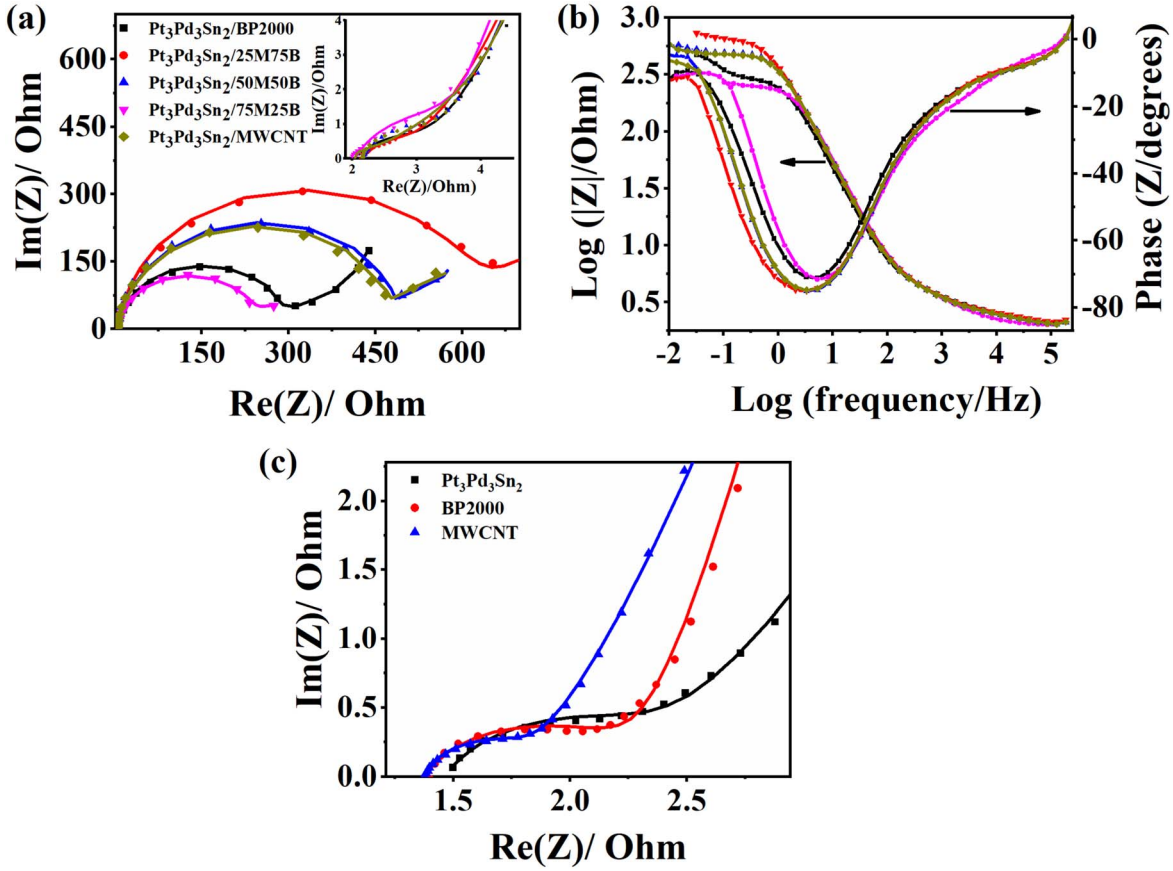

Figure 6. (a) Complex-plane impedance and (b) bode phase impedance plots recorded using $Pt_3Pd_3Sn_2$ supported on pure and mixed supports in a DME-saturated 0.5 M H_2SO_4 electrolyte. The inset in (a) is the semi-circle that appears at a high-frequency region. (b) Nyquist plot recorded using a carbon-free catalyst and catalyst-free carbons coated on Toray paper. (Nyquist plot recorded from 200 kHz to 10 m Hz at 0.8 V (vs NHE) with 6 frequencies per decade and 10 mV amplitude; catalyst loading of 100 μg cm^{-2}).

Table I. Simulated values of parameters in the equivalent circuit (in a DME-saturated solution at 0.8 V).

Catalyst	$Pt_3Pd_3Sn_2$/BP2000	$Pt_3Pd_3Sn_2$/25M75B	$Pt_3Pd_3Sn_2$/50M50B	$Pt_3Pd_3Sn_2$/75M25B	$Pt_3Pd_3Sn_2$/MWCNT
R_s (Ohm)	2.22	2.17	2.14	2.11	2.08
R_f (Ohm)	1.53	1.31	1.01	0.63	1.15
Q_f (F)	4.25×10^{-4}	3.74×10^{-4}	3.33×10^{-4}	3.20×10^{-4}	3.40×10^{-4}
R_{ct} (Ohm)	252	565	445	220	429
Q_{dl} (F)	7.00×10^{-4}	1.66×10^{-4}	1.80×10^{-2}	2.83×10^{-2}	5.98×10^{-3}
W_1(Ohm $s^{1/2}$)	42.45	45.86	45.75	42.38	40.58
X^2/|Z|	0.07	0.08	0.09	0.07	0.09

mixture. In all the frequency ranges, the minimum module of impedance (|Z|) shown by $Pt_3Pd_3Sn_2$/75M25B indicates the highest performance of the catalyst.[37] On the other hand, $Pt_3Pd_3Sn_2$/25M75B having the highest |Z| especially at the lower frequency region is related to its lowest activity. This is consistent with the electrochemical measurement results obtained for these catalysts in our previous work.[22]

Since the catalyst supported on the above supports is the same, the differences in the electrolyte, film, and charge transfer resistances are related to the support material's effect on the active metals. Hence, the effect of relevant applied electrode overpotentials and DME concentrations was further explored on the selected support materials as discussed in subsequent sections.

Potential effect.—Changing the electrode potential at which the impedance spectra are recorded affects the kinetic, mass transport, and diffusion regions of the DME polarization curve. The effect of the potential bias on the impedance spectra of the catalyst $Pt_3Pd_3Sn_2$/75M25B, that showed the highest peak current density (1.01 ± 0.06 mA cm^{-2}) and oxidation charge (395 ± 21.92 mC mg_{PGM}^{-1}) towards DME oxidation,[22] was studied by recording EIS at potentials between 0.2–1 V as shown in Fig. 7a and the corresponding Bode plot is presented in Fig. 7b. Except for the EIS recorded at 0.2 V, a similar equivalent circuit as to the one shown in Fig. 1 was used to fit the data. Since the second semicircle was not present in the EIS spectra measured at 0.2 V, the parallel $R_{ct}\|Q_{dl}$ was omitted from the equivalent circuit analysis. Excellent fitting results are confirmed from the minimal value of X^2/|Z| (Table II).

The solution resistance (R_s) obtained from the intercept of the real impedance at high frequency was almost independent of the potential bias when an aqueous solution of the same ionic concentration was used for all the potentials. Hence, the R_s values of all potentials are expressed relative to the resistance at 0.2 V. The resistance at the catalyst layer (R_f) depends on the applied electrode

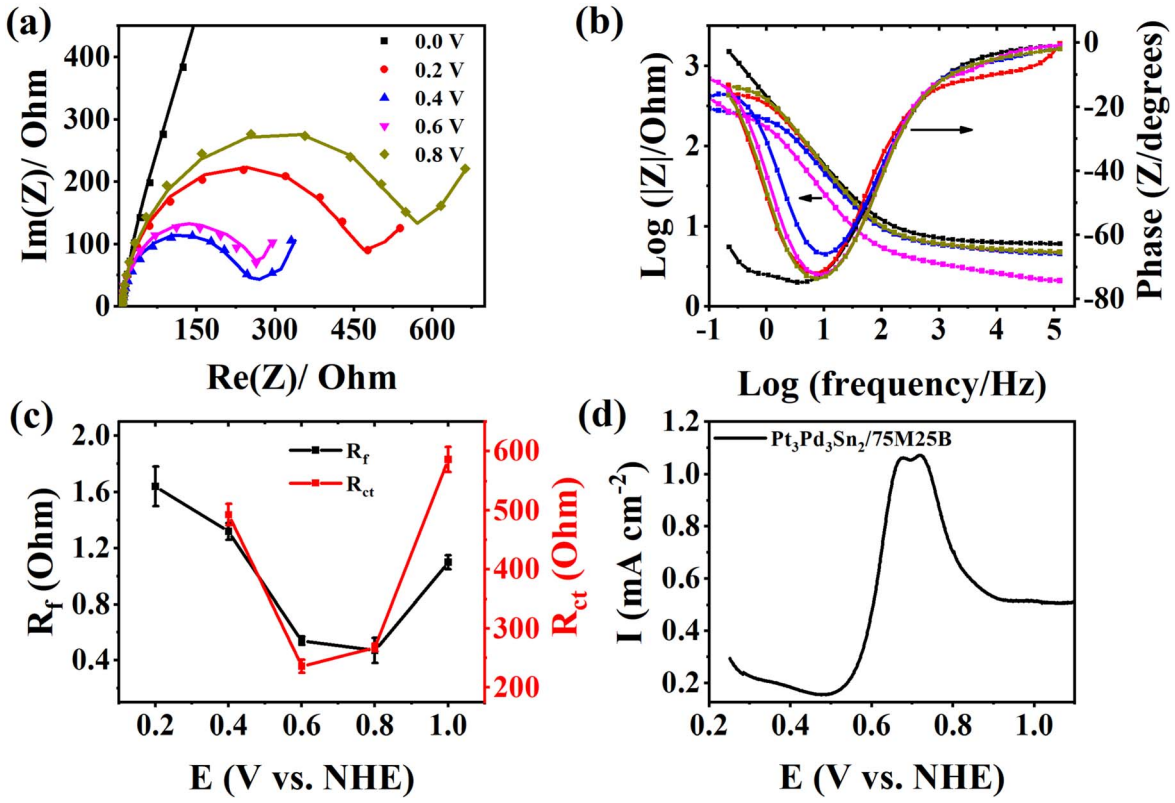

Figure 7. Effect of potential bias on the (a) Nyquist and (b) Bode impedance spectra recorded using $Pt_3Pd_3Sn_2$/75M25B. (c) Change in the values of R_f and R_{ct} vs applied potential. (d) LSV (10 mV s^{-1}) recorded using the catalyst (in DME-saturated 0.5 M H_2SO_4 electrolyte, 100 μg cm^{-2} catalyst loading).

Table II. Equivalent circuit fitted values at varying potentials.

Potential (V vs NHE)	0.2	0.4	0.6	0.8	1.0
R_s (Ohm)	2.32	2.30	2.20	2.16	2.22
R_f (Ohm)	1.64	1.32	0.74	0.67	1.10
R_{ct} (Ohm)	—	493	226	268	586
Q_{dl} (F)	—	4.74×10^{-2}	6.3×10^{-2}	7.8×10^{-2}	6.5×10^{-2}
W_1 (Ohm.$s^{1/2}$)	81.83	53.41	61.27	34.07	45.40
X^2/|Z|	0.02	0.09	0.08	0.08	0.05

potential affecting the transport of H^+ and SO_4^+ at the metal-metal and metal-support interfaces.[38,39] With an increase in the electrode potential, the diameter of the first semicircle decreased (R_f decreased) suggesting that the transfer of H^+ and SO_4^+ across/between the catalyst layer components was facilitated. The slight increase in the R_f at 1 V could be due to the formation of oxide species at high potentials that hinder these ions' movements (Fig. 7d).

Since the low applied potential of 0.4 V is far from the DME oxidation onset potential (0.5–0.55 V, Fig. 7d), the impedance mostly describes the charge transfer of proton adsorption/desorption on the DME-covered catalyst surface. In the absence of any significant DME oxidation at these potentials, stable molecular fragments such as CH_3, CH_2OH, and CO_{ads}[34] inhibit the proton adsorption/desorption kinetics, leading to a high value of R_{ct}.

The diameter of the second semicircle was small at 0.6 V and 0.8 V for the $Pt_3Pd_3Sn_2$/75M25B catalyst. This is ascribed to facile DME oxidation kinetics, consistent with higher current density shown in Fig. 7d at these potential regions, also supported by the smaller phase angles of the Bode plot observed at this potentials as compared to the other potentials (Fig. 7b). The previous report[1] on XC72-supported $Pt_3Pd_3Sn_2$ anode catalyst showed that the DME oxidation onset potential and the peak current density occur at around 0.6 V and 0.75 V, respectively. However, when supported on 75M25B, the onset potential shifted more than 70 mV to a lower potential and showed a higher current density at 0.7 V.[22] The low R_{ct} obtained at 0.6–0.8 V with 75M25B support also suggests a facile DME oxidation kinetics and better removal of the adsorbed DME oxidation intermediates such as CO_{ads}. The increase in the R_{ct} above 0.6 V was ascribed to the presence of a low concentration of surface adsorbed intermediates (diffusion-controlled process) followed by the formation of a thick oxide layer that prevented further adsorption and oxidation of DME. The lower R_{ct} at 0.4 V as compared to at 1 V (Fig. 7c), suggests that the passivation of the surface by the oxides formed at higher potentials poses more resistance than the kinetic limited process at lower potentials. It can be seen in Table II that the capacitive impedance (Q_{dl}) is higher in the potential region where DME oxidation occurs (0.6–1 V).

DME concentration effect.—Shown in Fig. 8a is the variation of the impedances with the change in the concentration of DME in the solution. The simulated values of the EEC elements are given in Table III. For the 0.74 M of DME, EIS has been recorded in a DME-saturated 0.5 M H_2SO_4 solution. The 20%–80% (0.15–0.59 M) of the saturated DME gas concentration was achieved by purging a required volume of N_2-saturated 0.5 M H_2SO_4 solution to the initially DME-saturated 0.5 M H_2SO_4 solution using a burette

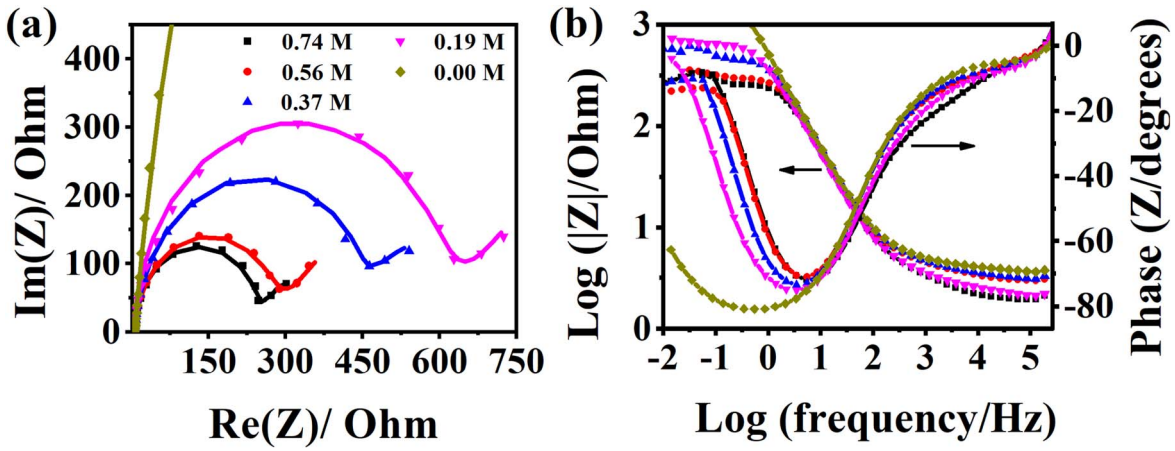

Figure 8. Effect of varying the DME concentration in 0.5 M H_2SO_4 on the (a) impedance (b) Bode spectra measured using a $Pt_3Pd_3Sn_2$/75M25B-coated electrode (Nyquist plot recorded from 200 kHz to 10 m Hz at 0.8 V with 6 frequencies per decades and 10 mV amplitude).

Table III. Simulated values of parameters in the equivalent circuit at varying DME concentration.

Concentration (M)	0.74	0.56	0.37	0.19
R_s (Ohm)	1.96	2.42	3.01	3.16
R_f (Ohm)	0.58	0.66	0.93	1.08
R_{ct} (Ohm)	226.6	255.3	413.7	565
Q_{dl} (F)	3.01×10^{-2}	3.65×10^{-3}	3.00×10^{-3}	2.90×10^{-3}
W_1 (Ohm.s$^{1/2}$)	35.27	44.09	55.03	49.97
X^2/|Z|	0.08	0.05	0.06	0.09

mounted to the three-electrode cell. The cell was completely sealed to prevent DME gas from escaping the solution. A similar EEC as in Fig. 1 was employed to fit the data with the simulation.

It can be seen from Table III that the electrolyte resistance, R_s, decreased with the increase in the DME concentration in the solution. This was due to the reduction in the surface tension of the solution making it less resistant to the flow of ions. Kumar et al.[40] studied the surface tension (τ) for a binary mixture of DME and water and observed that with an increase in the mole fraction of the DME, the τ of the mixture decreased. The first semicircle of the Nyquist plot (R_f) is not exclusively related to the DME oxidation since it was also present in the impedance spectra of the N_2-saturated 0.5 M H_2SO_4. However, the radius is shown to decrease with an increase in the DME concentration.

High DME concentration at the electrode/electrolyte interface improves the kinetics, lowering the kinetic charge transfer resistance, R_{ct}. It can be observed in Fig. 8a that with an increase in the DME concentration in the solution, the diameter of the second semicircle (R_{ct}) decreases in agreement with the surface coverage by DME and faster anodic reaction kinetics. EIS studies by Danaee et al.[41] and Ekdharmasuit et al.[42] conducted on electrooxidation of varying concentrations of methanol and ethanol, respectively, showed similar observations. The highest Q_{dl} at 0.74 M of DME is associated with the highest charge that could be provided by saturating the solution with DME.

The corresponding phase angle and impedance module plots at varying concentrations of DME oxidation are shown in Fig. 8b. At 0 M DME, the phase angle doesn't show a clear peak. However, with an increase in the DME concentration in the electrolyte, the phase angle decreases and shifts to a higher frequency which indicates an enhancement in the DME oxidation kinetics.[43,44]

DME oxidation kinetics.—To the best of our knowledge, DME oxidation kinetics on any catalyst-coated electrode surface has not been reported. In this study, we have calculated the DME oxidation kinetic parameters (reaction order (n) and rate constant (k), and DME diffusion coefficient (D_{DME})) from the EIS measurements. To determine n and k, an exchange current density (j_o) was initially computed for each R_{ct} (resistance associated with the DME oxidation) obtained at varying DME concentrations (C) at 0.6 V (Fig. 8a) according to the linearized Butler-Volmer Eq. 8.

$$j_0 = \frac{RT}{zFAR_{ct}} \quad [8]$$

Where R, T, z, F, and A are the universal gas constant (J mol^{-1} K^{-1}), reaction temperature (K), number of electrons transferred, Faraday's constant (C mol^{-1}), and the electrode area (cm^2), respectively. Here, we have assumed a complete DME oxidation for the z as the potential applied (0.8 V) is high enough to oxidize all the reaction intermediates formed.

The j_o is related to the C by Eq. 9

$$j_o = \frac{kC^n}{A} \quad [9]$$

Combining equating Eqs. 8 and 9 and taking the log of the resulting equation yields the following Eq. 10

$$\log R_{ct} = -n \log C + \log\left(\frac{RT}{zFk}\right) \quad [10]$$

Hence, a plot of log R_{ct} and Log C displayed in Fig. 9a gives a straight line with a slope n and y-intercept log (ART/zFk). Accordingly, the calculated n and k values are 0.68 and 1.10×10^{-5}, respectively. The value of n for the DME oxidation on $Pt_3Pd_3Sn_2$/75M25B calculated in this study is slightly higher than a previously reported value for DME combustion on Pt supported on Zeolite Socony Mobil–5 (Pt/ZSM-5).[45] The lower n obtained on Pt/ZSM-5 could be due to the high temperature (80 °C–150 °C) applied during the thermal combustion.

The DME diffusion coefficient (D_{DME}) was also calculated from the low-frequency linear part of the Nyquist plot (Warburg impedance) (Fig. 8a). The real or imaginary component of the Warburg

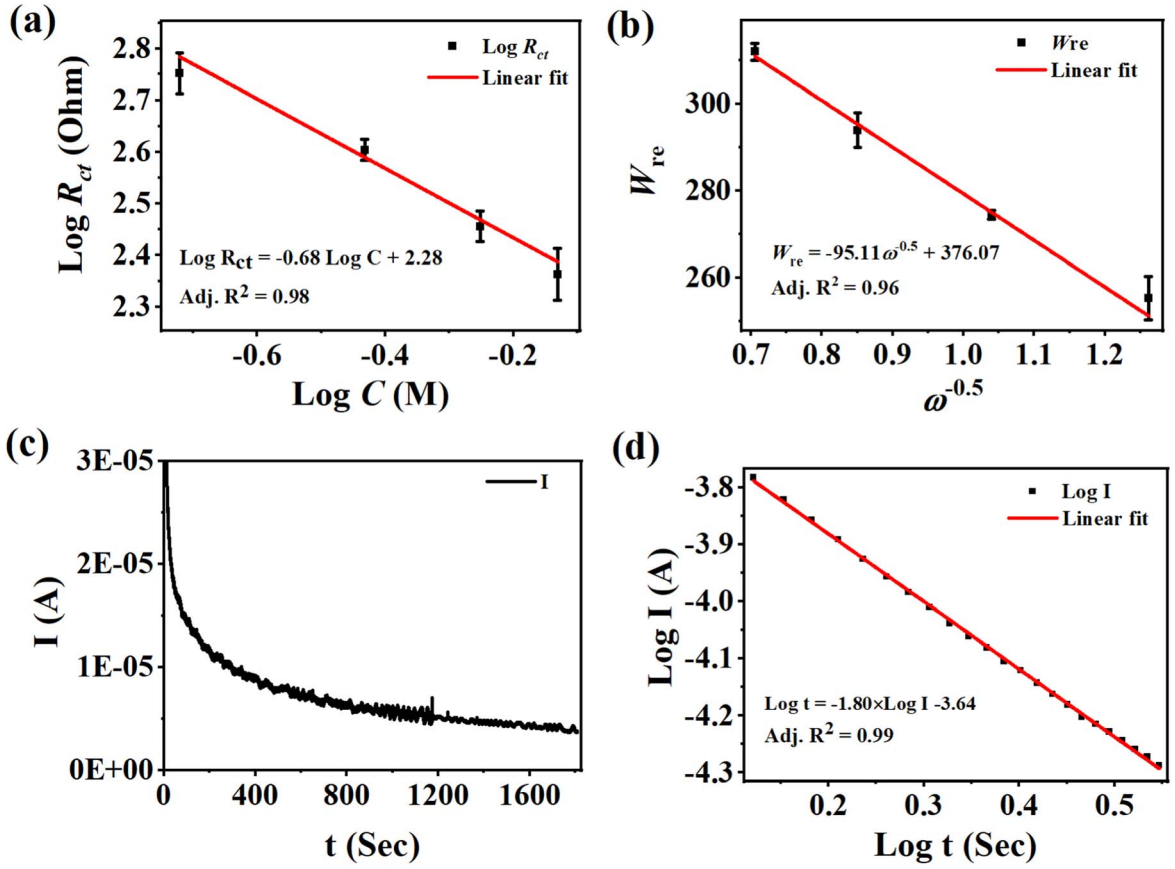

Figure 9. (a) a plot of Log C vs Log j_o to determine n and k of DME oxidation. (b) a plot of $\omega^{-0.5}$ vs W_{re} to compute D_{DME}. (c) a 30 min CA recorded in DME-saturated 0.5 M H_2SO_4 at 0.6 V using $Pt_3Pd_3Sn_2$/75M25B anode catalyst. (d) a plot of Log I vs Log I at the first few seconds of the CA.

impedance (W_{re} or W_{im}) is inversely related to the square root of angular frequency ($\omega^{-0.5}$). Therefore, a plot of W_{re} vs $\omega^{-1/2}$ gives a straight line as shown in Fig. 9b, with a slope of the Warburg coefficient (σ). The D_{DME} could then be calculated from σ using Eq. 11.

$$D_{DME}(EIS) = \frac{R^2T^2}{2A^2z^4F^4C^2\sigma^2} \quad [11]$$

Where *R, T, A, z, F,* and *C* are the ideal gas constant, absolute temperature (298 K), electrode surface area, the number of electrons transferred, Faraday's constant, and the concentration of the oxidizing species, respectively.

The D_{DME} computed from the Warburg impedance was compared with the D_{DME} determined from a chronoamperometry (CA) (Fig. 9c) recorded at the same potential and catalyst loading (0.6 V and 100 μg cm^{-2}) using the Cottrell Eq. 12.

$$I = \frac{zAFC\sqrt{D_{DME}}}{\sqrt{\pi}\sqrt{t}} \quad [12]$$

The D_{DME} computed from the EIS and CA were in the same orders of magnitude (1.07×10^{-13} and 2.25×10^{-13} cm^2 s^{-1}, respectively). This value is lower than the reported diffusion coefficients of liquid fuels such as methanol and ethanol which are in the order of 10^{-9} and 10^{-10} cm^2 s^{-1}, respectively.[46,47]

Conclusions

The role of support materials on the activity of a catalyst ($Pt_3Pd_3Sn_2$) was studied using electrochemical impedance spectroscopy (EIS) coupled with various physico-chemical characterization techniques such as XRD, SAXS, and STEM. To this end, the catalyst was supported on a single and a combination of MWCNT and BP2000 carbon supports. Even though better dispersion and particles of smaller size were observed on pure BP2000, their confinement in the support pores makes them inaccessible to the DME fuel. On the other hand, the positive advantage of better fuel accessibility by the particles due to their deposition on the sidewalls of the MWCNT tubes was counterbalanced by the presence of large and agglomerated particles. Mixing the two carbon supports in appropriate proportions allowed for obtaining catalysts of optimized particle size, surface area, dispersion, and conductivity. A facile movement of protons and SO_4^+ ions was observed among the catalyst layer components for the 75M25B-supported $Pt_3Pd_3Sn_2$-coated electrode. This was ascribed to the conductive nature of the support. Moreover, the smallest charge transfer resistance at the electrode/electrolyte interface (R_{ct}) for $Pt_3Pd_3Sn_2$/75M25B suggests the role of the optimized support in enhancing the catalyst activity towards DME oxidation and better removal of oxidation intermediates.

Acknowledgments

The authors would like to greatly acknowledge Ariel University for financially supporting this research work.

ORCID

Hannan Teller https://orcid.org/0000-0002-1819-9180
Alex Schechter https://orcid.org/0000-0002-3464-1936

References

1. D. Kashyap, H. Teller, P. Subramanian, B. Petr, M. G. Gebru, I. Pitussi, R. S. Yadav, H. Kornweitz, and A. Schechter, *J. Power Sources*, **544**, 231882 (2022).
2. K. Oshita, M. Takaoka, S. Ichiro Kitade, N. Takeda, H. Kanda, H. Makino, T. Matsumoto, and S. Morisawa, *Chemosphere*, **78**, 1148 (2010).

3. D. Kashyap, H. Teller, and A. Schechter, *ChemElectroChem*, **6**, 2407 (2019).
4. Z. Wang, H. Fan, H. Liang, J. Ma, S. Li, Y. Song, and R. Wang, *Electrochim. Acta*, **230**, 245 (2017).
5. I. Vincent, A. Kruger, and D. Bessarabov, *Int. J. Hydrogen Energy*, **42**, 10752 (2017).
6. G. Mirshekari, R. Ouimet, Z. Zeng, H. Yu, S. Bliznakov, L. Bonville, A. Niedzwiecki, C. Capuano, K. Ayers, and R. Maric, *Int. J. Hydrogen Energy*, **46**, 1526 (2021).
7. D. Bhalothia, Y. J. Fan, T. H. Huang, Z. J. Lin, Y. T. Yang, K. W. Wang, and T. Y. Chen, *J. Phys. Chem. C*, **123**, 19013 (2019).
8. C. Liang, L. Ding, C. Li, M. Pang, D. Su, W. Li, and Y. Wang, *Energy Environ. Sci.*, **3**, 1121 (2010).
9. D. Kashyap, H. Teller, and A. Schechter, *J. Power Sources*, **396**, 335 (2018).
10. B. M. Babić, L. M. Vračar, V. Radmilović, and N. V. Krstajić, *Electrochim. Acta*, **51**, 3820 (2006).
11. B. Thirumalraj, C. Rajkumar, S. M. Chen, P. Veerakumar, P. Perumal, and S. Bin Liu, *Sensors Actuators, B Chem*, **257**, 48 (2018).
12. R. Mohan, A. Modak, and A. Schechter, *ACS Sustain. Chem. Eng.*, **7**, 11396 (2019).
13. C. Y. Wu, P. W. Wu, and P. Lin, *J. Power Sources*, **195**, 5122 (2010).
14. A. Ishihara, M. Chisaka, Y. Ohgi, K. Matsuzawa, S. Mitsushima, and K. Ota, *Phys. Chem. Chem. Phys.*, **17**, 7643 (2015).
15. H. C. Honig, A. Friedman, N. Zion, and L. Elbaz, *Chem. Commun.*, **56**, 8627 (2020).
16. D. N. Kärger and J. Ruthven, *D. M., & Theodorou* (Wiley, New York) (2012).
17. B. A. Johnson, A. M. Beiler, B. D. McCarthy, and S. Ott, *J. Am. Chem. Soc.*, **142**, 11941 (2020).
18. E. Najafli, S. Ratso, Y. P. Ivanov, M. Gatalo, L. Pavko, C. R. Yörük, P. Walke, G. Divitini, N. Hodnik, and I. Kruusenberg, *ACS Appl. Nano Mater.*, **6**, 5772 (2023).
19. L. H. Xing, G. P. Yin, Z. B. Wang, S. Zhang, Y. Z. Gao, and C. Y. Du, *J. Power Sources*, **198**, 170 (2012).
20. M. Chen, C. Y. Du, G. P. Yin, P. F. Shi, and T. S. Zhao, *Int. J. Hydrogen Energy*, **34**, 1522 (2009).
21. X.- Z. Yuan, C. Song, H. Wang, and J. Zhang, *Electrochemical Impedance Spectroscopy in PEM Fuel Cells* (Springer London Dordrecht Heidelberg New York)(Springer London)p. 1 (2010).
22. M. G. Gebru, H. Teller, P. Subramanian, and A. Schechter, *Energy Technol.*, **2200835**, 1 (2022).
23. E. O. Balogun, N. Hussain, J. Chamier, and P. Barendse, *Int. J. Hydrogen Energy*, **44**, 32219 (2019).
24. V. B. Kumar, D. Kashyap, H. Teller, M. G. Gebru, A. Gedanken, and A. Schechter, *Mater. Today Sustain.*, **17**, 100095 (2022).
25. X. Zhao et al., *J. Mater. Chem. A*, **8**, 1368 (2020).
26. K. Bergamaski, A. L. N. Pinheiro, E. Teixeira-Neto, and F. C. Nart, *J. Phys. Chem. B*, **110**, 19271 (2006).
27. T. Frelink, W. Visscher, and J. A. R. van Veen, *J. Electroanal. Chem.*, **382**, 65 (1995).
28. J. Zhuang, D. Gu, L. Xi, K. Lin, and Y. Fang, *Powder Technol.*, **368**, 59 (2020).
29. S. Hussain, H. Erikson, N. Kongi, M. Merisalu, M. Rähn, V. Sammelselg, G. Maia, and K. Tammeveski, *J. Electrochem. Soc.*, **164**, F1014 (2017).
30. A. G. Kikhney and D. I. Svergun, *FEBS Lett.*, **589**, 2570 (2015).
31. L. Wu, H. Lian, J. J. Willis, E. D. Goodman, I. S. McKay, J. Qin, C. J. Tassone, and M. Cargnello, *Chem. Mater.*, **30**, 1127 (2018).
32. M. O. Londono, P. Tancredi, D. Muraca, L. M. Socolovsky, and M. Knobel, "Small-Angle X-Ray Scattering to Analyze the Morphological Properties of Nanoparticulated Systems." *Handbook of Materials Characterization*, ed. S. K. Sharma (Gewerbestrasse 11, 6330 Cham, Switzerland)(Springer International Publishing) (2018).
33. B. Bera, T. Kar, A. Chakraborty, and M. Neergat, *J. Electroanal. Chem.*, **805**, 184 (2017).
34. J. A. Herron, P. Ferrin, and M. Mavrikakis, *J. Phys. Chem. C*, **118**, 24199 (2014).
35. J. Huang, Z. Li, B. Y. Liaw, and J. Zhang, *J. Power Sources*, **309**, 82 (2016).
36. M. E. G. Lyons and M. P. Brandon, *J. Electroanal. Chem.*, **631**, 62 (2009).
37. A. Gharib and A. Arab, *Int. J. Hydrogen Energy*, **46**, 3865 (2021).
38. J. Kunze-Liebhäuser, A. S. Bandarenka, A. Auer, and X. Ding, *J. Phys. Chem. C*, **125**, 5020 (2021).
39. A. A. Kornyshev, A. M. Kuznetsov, and J. Ulstrup, *J. Phys. Chem.*, **98**, 3832 (1994).
40. A. Kumar, V. P. Mohandas, and P. K. Ghosh, *J. Chem. Eng. Data*, **48**, 1318 (2003).
41. I. Danaee, M. Jafarian, F. Forouzandeh, F. Gobal, and M. G. Mahjani, *Int. J. Hydrogen Energy*, **34**, 859 (2009).
42. P. Ekdharmasuit, A. Therdthianwong, and S. Therdthianwong, *Int. J. Hydrogen Energy*, **39**, 1775 (2014).
43. D. Y. Chung, K. J. Lee, and Y. E. Sung, *J. Phys. Chem. C*, **120**, 9028 (2016).
44. S. Sun and Z. J. Xu, *Electrochim. Acta*, **165**, 56 (2015).
45. C. Deng, W. Yang, J. Zhou, Y. Wang, Z. Wang, and K. Cen, *Catal. Commun.*, **84**, 48 (2016).
46. J. Li et al., *J. Mater. Chem. A*, **7**, 22036 (2019).
47. A. Eshghi, E. Sadati Behbahani, M. Kheirmand, and M. Ghaedi, *Int. J. Hydrogen Energy*, **44**, 28194 (2019).